

Electrically Pumped Orbital Angular Momentum (OAM) Laser at Telecom Wavelengths

Juan Zhang^{1,*}, Changzheng Sun^{1,*}, Bing Xiong¹, Jian Wang¹, Zhibiao Hao¹, Lai Wang¹, Yanjun Han¹, Hongtao Li¹, Yi Luo¹, Yi Xiao², Chuanqing Yu², Takuo Tanemura², Yoshiaki Nakano², Shimao Li³, Xinlun Cai³, Siyuan Yu³

¹Laboratory for Information Science and Technology, State Key Lab on Integrated Optoelectronics, Department of Electronic Engineering, Tsinghua University, Beijing 100084, China

²Integrated Photonics Laboratory, Department of Electrical Engineering and Information Systems, Graduate School of Engineering, the University of Tokyo, Tokyo 113-8656, Japan

³State Key Laboratory of Optoelectronic Materials and Technologies and School of Physics and Engineering, Sun Yat-sen University, Guangzhou 510275, China.

*Theses authors contributed equally to this work. Correspondence and requests for materials should be addressed to Y. L. (luoy@tsinghua.edu.cn), or to Y. N. (nakano@hotaka.t.u-tokyo.ac.jp) or to X. C. (caixlun5@mail.sysu.edu.cn).

Semiconductor lasers capable of generating a vortex beam with a specific orbital angular momentum (OAM) order are highly attractive for applications ranging from nanoparticle manipulation, imaging and microscopy to fibre and quantum communications. In this work, an electrically pumped OAM laser operating at telecom wavelengths is fabricated by monolithically integrating an optical vortex emitter with a distributed feedback (DFB) laser on the same InGaAsP/InP epitaxial wafer. A single-step dry etching process is adopted to complete the OAM emitter, equipped with specially designed top gratings. The vortex beam emitted by the integrated laser is captured, and its OAM mode purity characterized. The electrically pumped OAM laser eliminates the external laser required by silicon- or silicon-on-insulator (SOI)-based OAM emitters, thus demonstrating great potential for applications in communication systems and quantum domain.

Optical vortex beams with a helical wave front are known to carry orbital angular momentum (OAM)¹. The phase of an OAM-carrying beam varies with the azimuthal angle ϕ , i.e., $E \sim \exp(jl\phi)$, where l is the topological charge of the OAM state^{1,2}. OAM offers a new degree of freedom for information transmission, in addition to the already extensively exploited wavelength, amplitude, phase, and polarization. It holds the potential for enhancing the capacity and spectral efficiency of optical communication systems, as there are theoretically an unbounded number of orthogonal states^{2,3}. In addition to the impressive demonstrations of their capacity in free-space and fibre communications⁴⁻⁶, beams carrying OAM have also attracted substantial attention for myriad applications^{7,8}, including optical manipulation⁹⁻¹¹, imaging and microscopy^{12,13}, and quantum information^{14,15}.

Compared with the bulky optical components typically used for OAM beam generation, such as spiral phase plates¹⁶, cylindrical lens-based mode converters¹⁷ or forked holograms implemented with spatial light modulators (SLMs)¹⁸, chip-based optical vortex emitters offer a much more compact and robust solution. To date, most chip-scale OAM beam emitters are based on silicon or silicon-on-insulator (SOI) wafers¹⁹⁻²², which are attractive because of the strong optical confinement and mature fabrication technology. However, the indirect bandgap of silicon means that an external laser must be employed to pump the OAM emitter, thus making monolithically integrated OAM emitters impossible.

Different approaches to realizing monolithic OAM lasers have also been reported. An OAM laser can be realized by fabricating a micro-scale spiral phase plate within the aperture of a vertical-cavity surface-emitting laser (VCSEL)²³. Unfortunately, the laser emits light at approximately 860 nm, which is not a telecom wavelength. Optical vortex emission at 1550 nm is demonstrated with a microlaser capable of precise control of the topological charge by taking advantage of the exceptional point formed by complex refractive index modulation²⁴. However, the device is optically pumped, which limits its practical applications in telecommunications. A monolithically integrated electrically pumped continuous-wave OAM laser operating at 1550 nm is highly desirable for OAM-based telecommunications.

In this work, an electrically pumped OAM laser operating at telecom wavelengths is demonstrated for the first time. The device is fabricated on an InGaAsP/InP multiple quantum well (MQW) epitaxial wafer by monolithically integrating a microring-based optical vortex emitter with a distributed feedback (DFB) semiconductor laser. The electrically pumped device can emit OAM beam with high mode purity, making it attractive for applications in fibre communications or quantum information.

Results

Device structure. Microring resonator is likely the most efficient structure for OAM beam generation. For example, an OAM beam is generated and emitted by the same microring structure in a microlaser²⁴. However, the symmetry of the ring resonator normally leads to simultaneous generation of clockwise (CW) and counterclockwise (CCW) whispering gallery modes (WGMs), and special attention must be paid to avoid mode degeneracy²⁴.

In this work, a microring-based optical vortex emitter is monolithically integrated with a single-mode laser diode on InP substrate, representing the first demonstration of an electrically pumped OAM laser at telecom wavelengths. As shown in Fig. 1a, light from the DFB laser is coupled into the optical vortex emitter, and an OAM-carrying beam will be emitted vertically once the light is on resonance within the microring. Because light is unidirectionally coupled into the microring, only the CCW mode is excited, thus avoiding mode degeneracy in the WGM resonator.

Compared with OAM emitters based on a circular grating coupler²⁰ or a microring resonator with download units^{21,22}, optical vortex emitters based on a microring with angular gratings are highly compact. The radius of the microring can only be a few microns long, making the device particularly attractive for dense photonic integration¹⁹. Furthermore, OAM

beams with high mode purity can be obtained easily by increasing the number of grating elements²⁵. In this work, we adopt azimuthal gratings formed on top of the ring waveguide to extract phase-coherent beam from the WGM in the ring. OAM-carrying beams are generated when the following angular phase-matching condition is satisfied¹⁹

$$l = M - N \quad (1)$$

where l , M , and N are all integers, with l being the topological charge of the OAM state, N the number of total grating elements, and M the azimuthal resonant order of the WGM.

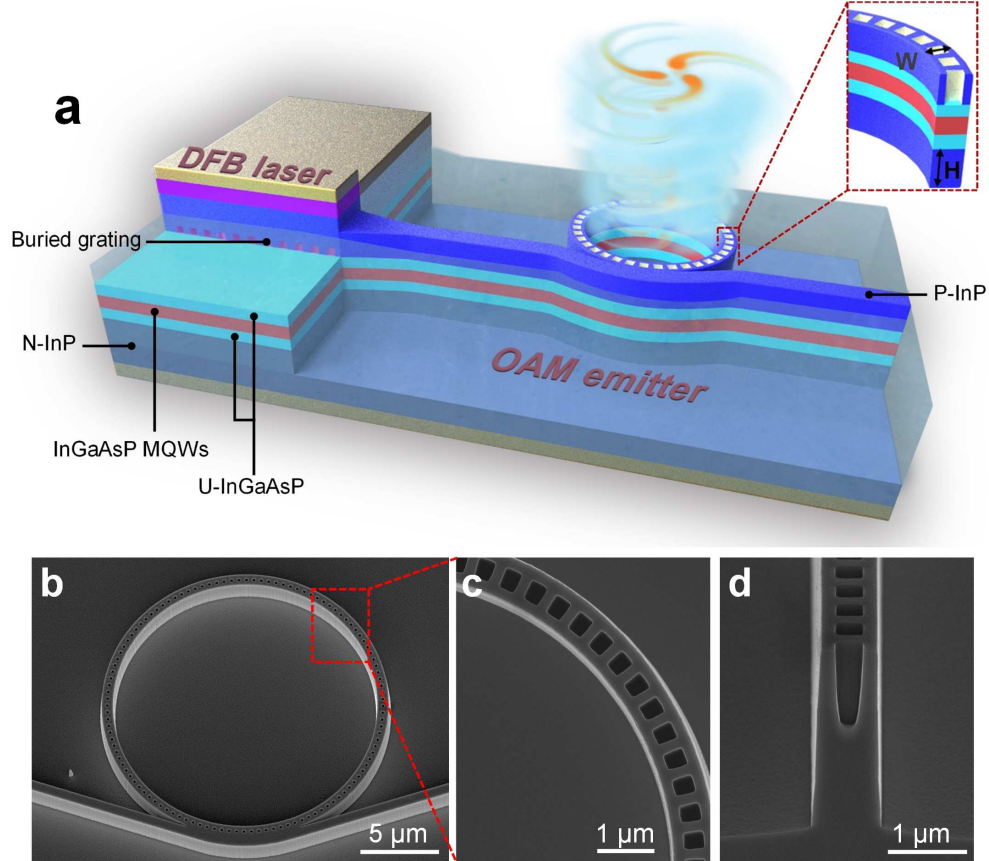


Figure 1 | Integrated orbital angular momentum laser. (a) Integrated OAM laser with shallow-etched DFB laser and deeply etched vortex emitter on InGaAsP/InP wafer. Inset reveals the cross-section of the vortex emitter. (b) SEM image of the fabricated OAM emitter, (c), (d) top and cross-sectional view of the top-grating structure.

As shown in Fig. 1a, the 400- μm -long DFB laser is processed into a shallow-etched ridge waveguide structure, with compressively strained InGaAsP MQWs as the active layer. On the other hand, the 9.56- μm -radius optical vortex emitter adopts a deeply etched ridge structure to ensure strong optical confinement, thus allowing a small ring radius to reduce absorption loss in the ring resonator. To further reduce the absorption loss of the vortex emitter, we adopt the identical epitaxial layer integration scheme with a properly red-detuned lasing wavelength²⁶. Thus, the lasing wavelength of the DFB laser lies outside the high absorption range of the InGaAsP MQW active layer, while sufficient gain can be maintained for the lasing mode because of carrier-induced bandgap shrinkage (see Methods). Consequently, both the DFB

laser and the vortex emitter can be formed on the same epitaxial layer, without the need for additional regrowth.

The inset of Fig. 1a depicts the geometry of the deeply etched ring waveguide. The mode profile within the ring depends critically on the width and height of the ridge waveguide. A ridge width W of $0.8\ \mu\text{m}$ is adopted to ensure single-mode operation. Moreover, the distance between the ridge bottom and the lower bound of the InGaAsP cladding layer, denoted by H , should be at least $1\ \mu\text{m}$ to ensure negligible optical leakage into the InP substrate²⁷. Blind-hole-like grating elements measuring $0.4 \times 0.3\ \mu\text{m}^2$ are etched into the top of the ring waveguide to generate vertical OAM radiation by scattering the radial component E_r of the WGM in the ring (see Methods). Fig. 1b shows a scanning electron microscopy (SEM) image of the OAM laser with top gratings fabricated on the InGaAsP/InP epitaxial wafer. As shown in Fig. 1d, the depth of the top gratings is controlled such that the MQW active layer remains intact. A total of $N = 116$ grating elements are formed on the $9.56\text{-}\mu\text{m}$ -radius WGM resonator, corresponding to a resonance order $M = 120$ at $\sim 1544\ \text{nm}$.

L-I characteristics and polarization. In Fig. 2a, the optical power collected at the DFB laser facet and vertical to the OAM emitter is plotted against the current injected into the DFB laser²⁷, indicating a threshold current of approximately 51 mA. The insets illustrate the near-field patterns of the OAM laser at pump currents near and above the threshold. As illustrated in Fig. 2b, the wavelength of the DFB laser is approximately 1544 nm at an injection current of 60 mA.

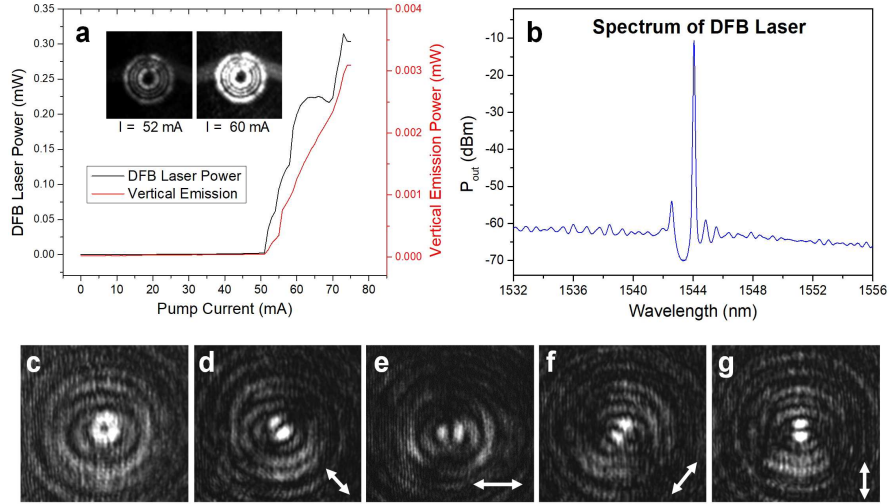


Figure 2 | L-I characteristics and polarization. (a) L-I characteristics of DFB laser output power (black) and OAM emission (red). Insets show near-field patterns of the integrated OAM laser at different pumping currents. (b) Spectrum of DFB laser. (c) Intensity distribution of the emitted beam. (d-g) Intensity distributions with the polarization indicated by the arrows.

Fig. 2c shows the far-field intensity distribution of the vertically emitted beam recorded with an infrared charge-coupled device (IR-CCD). The concentric annular pattern with a dark centre is characteristic of an OAM-carrying beam¹⁹. Theoretical analysis predicts radially polarized emission because of the scattering of E_r by top gratings²⁷. To verify the polarization, we measured the intensity distribution after a linear polarizer with the polarization orientation indicated by arrows shown in Figs. 2d-2g. It is evident that the two-lobed pattern is parallel to the polarizer axis, confirming radial polarization of the radiated beam.

OAM mode characterization. The OAM beam radiated by gratings on the WGM resonator can be expressed in terms of the Jones vector as^{25,28}

$$\mathbf{E} = E_{c1} \exp[j(l+1)\varphi] \begin{pmatrix} 1 \\ -j \end{pmatrix} + E_{c2} \exp[j(l-1)\varphi] \begin{pmatrix} 1 \\ j \end{pmatrix}, \quad (2)$$

which is composed of a right-hand circularly polarized (RHCP) OAM beam with topological charge $l + 1$ and a left-hand circularly polarized (LHCP) OAM beam with topological charge $l - 1$ ^{19,25}. To obtain a pure OAM mode, a polarization filter can be used to select the RHCP or LHCP component of the beam²⁹.

To verify the topological order and the mode purity, we demodulated the OAM beam by a spatial light modulator (SLM) encoded with different orders of helical phase^{29,30}. Figure 3 shows the setup used to determine the topological charge of the OAM beam. The OAM laser is pumped by a direct current (DC) source, and the OAM-carrying beam is collimated by an objective lens. The LHCP or RHCP component of the beam is selected when the 1/4 waveplate is set to +45 or -45 degrees relative to the axis of the polarizer. The beam is then demodulated and reflected by the SLM and finally projected onto an IR-CCD. The topological charge of the OAM carrying beam can be determined by varying the order of the holographic pattern loaded onto the SLM.

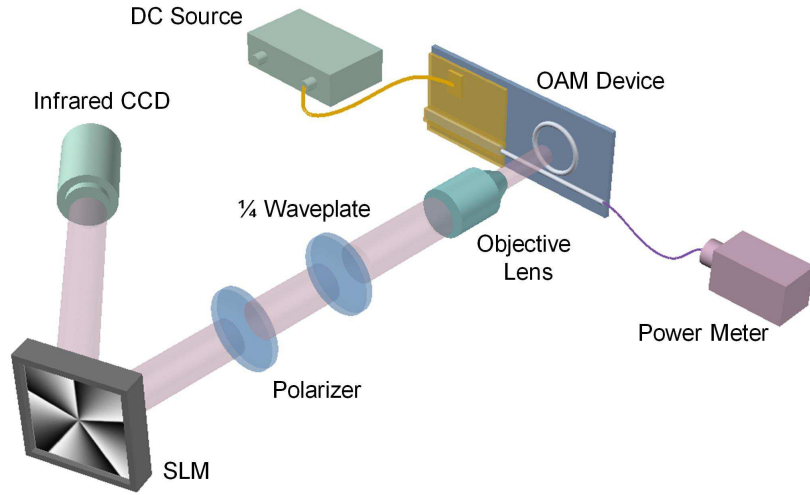


Figure 3 | Experimental setup for measuring topological charge and mode purity of the OAM beam.

As shown in the first row of Fig. 4a, the OAM order of the RHCP component is found to be +5, as a bright spot at the centre appears when the beam is reflected by the SLM with a -5-order holographic phase pattern. On the other hand, the OAM order of the LHCP component is +3. According to equation (2), the l value of this OAM laser is +4.

With the help of the SLM, the mode purity of the emitted OAM beam can also be measured. Here, the OAM mode purity is defined as the relative central intensity of the beam after demodulation by the SLM with opposite OAM order^{29,30}. As illustrated in Fig. 4b, the mode purity values of the RHCP and LHCP components are determined to be 0.76 and 0.85, respectively. For our integrated OAM laser, the degradation of mode purity may result from the mismatch between the lasing wavelength and the WGM resonator resonance. Wavelength matching could be fulfilled by either tuning the wavelength of the DFB laser or adjusting the effective refractive index of the WGM resonator by microheaters²⁹.

To determine the ideal mode purity attainable with our OAM laser, i.e., mode purity under wavelength matching, we send the light from a tuneable laser into the OAM emitter without electrically pumping the laser and demodulate the vertically emitted beam with an SLM. Figures 4c and 4d plot the OAM mode purity of different OAM orders obtained by adjusting

the incident laser wavelength to coincide with that of the corresponding resonance. The histograms indicate that for our OAM emitter, a mode purity higher than 0.8 for most modes could be realized upon wavelength matching.

The inhomogeneous light intensity in the WGM resonator is another important factor leading to degraded OAM mode purity²⁵. As light propagates inside the WGM resonator, the intensity of the light will gradually decrease because of various loss mechanisms, including the scattering of the grating and absorption of the III-V material. This degradation can be alleviated by optimizing the coupling structure, adjusting the geometry of the grating elements³¹, and electrically pumping the WGM resonator.

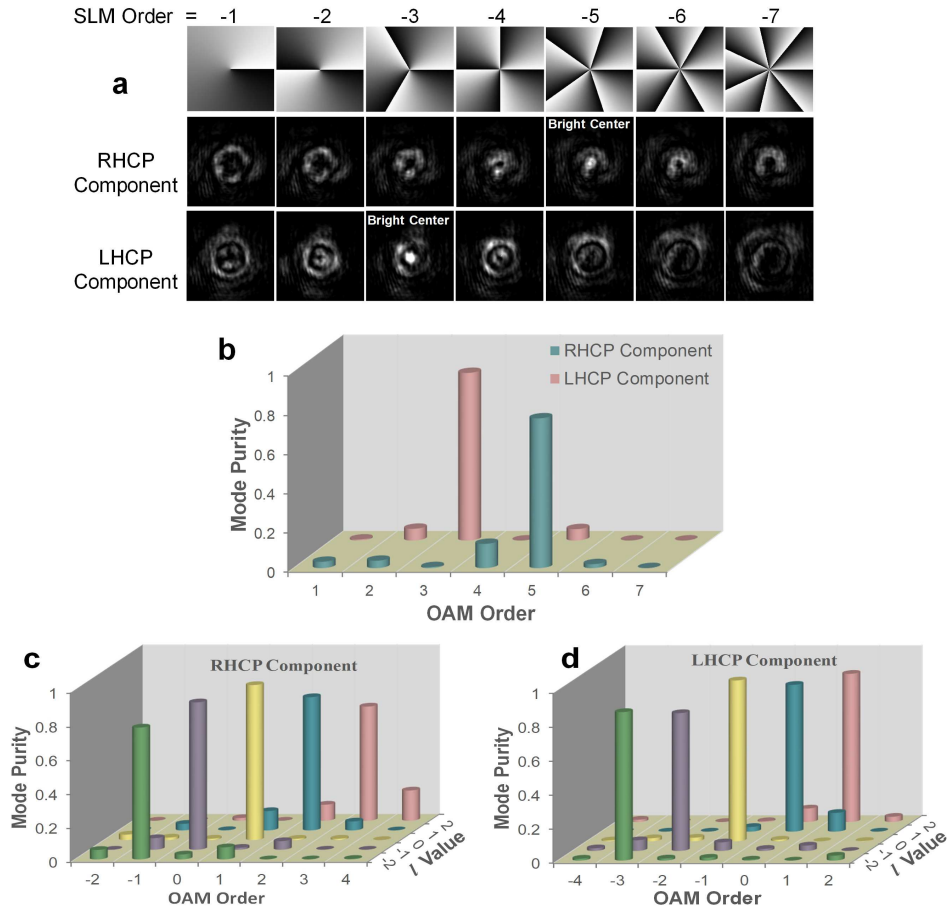


Figure 4 | OAM mode characterization. (a) OAM lasing modulated by SLM. The first row shows holograms of the SLM. The second and third rows are patterns of the RHCP and LHCP components after being reflected by the SLM in the first row, indicating $l = +4$. (b) Mode purities of the OAM lasing measured by the SLM. (c) Mode purities of the RHCP and (d) LHCP components of the OAM-carrying beams radiated by the OAM emitter.

Discussion

An electrically pumped integrated OAM laser at telecom wavelengths is realized for the first time. The DFB laser integrated optical vortex emitter allows unidirectional WGM excitation in the microring resonator, thus effectively avoiding mode degeneracy. The optical vortex emitter is equipped with a unique top grating structure, which enables efficient OAM radiation in the vertical direction. As a result, OAM lasing with specific topological charge is

demonstrated. In addition, the InP-based integrated OAM laser is highly compact, as the size of the deeply etched WGM resonator can be reduced to the micron level.

The integrated OAM laser eliminates the external laser required by silicon- or SOI-based vortex emitters and thus opens a path toward large-scale integration. Furthermore, the topological charge of the OAM beam can be tuned either by adjusting the wavelength of the DFB laser or by thermally tuning the microring, which would greatly broaden its applications.

Methods

Principle of top gratings.

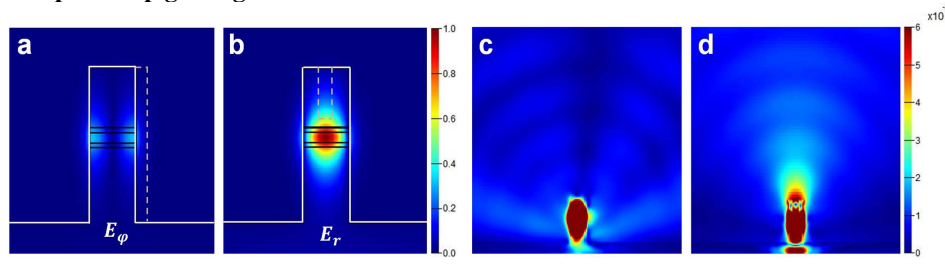


Figure 5 | Electric field and radiation of gratings. (a) Azimuthal electric field component E_ϕ and (b) transverse electric field component E_r for the quasi-TE mode in deeply etched straight waveguide at 1550 nm. (c, d) Radiation pattern of a 20- μm -long waveguide with sidewall gratings and top gratings, normalized to the power in the waveguide.

The efficiency of the OAM emission critically depends on the location of the grating elements. In previously reported SOI-based vortex emitters, angular gratings are positioned on the sidewall of the ring, as the strongly confined silicon waveguide features a significant azimuthal component E_ϕ at the sidewall¹⁹. In the deeply etched InP waveguide, however, the component E_ϕ at the sidewall is relatively weak, as shown in Fig. 5a. Furthermore, our simulations reveal that if gratings are fabricated on the sidewall, as depicted by the dashed line in Fig. 5a, a considerable portion of scattered light will be radiated laterally, dissipating into nearly horizontal emission²⁷, as shown in Fig. 5c.

On the other hand, Fig. 5b reveals a strong radial component E_r at the centre of the waveguide. If grating elements are formed on the top of the waveguide and etched down to near the active layer, as indicated by the dashed line in Fig. 5b, E_r will be scattered to produce vertical emission, resulting in a radially polarized OAM-carrying beam²⁷. This emission is achieved by forming a series of grating holes etched through the top InP cladding layer, just shy of the active layer, as illustrated in Figs. 1a and 1d. The simulation results shown in Fig. 5d confirm dominant vertical emission due to the top gratings.

Device fabrication. During device fabrication, buried gratings are formed in the DFB laser section through two-step epitaxial growth²⁶. The grating pitch is judiciously chosen to ensure that the Bragg wavelength of the DFB laser is redshifted from the photoluminescence peak of the compressively strained InGaAsP MQW active layer by approximately 45 nm. The DFB laser section is then processed into a standard ridge waveguide structure, with the width and height of the ridge being 2 μm and 1.95 μm , respectively. As depicted in Fig. 1a, the ohmic contact layer and part of the top InP cladding layer over the vortex emitter section are removed to reduce the absorption and scattering loss of the top gratings. The height of the deeply etched vortex emitter is approximately 2.1 μm .

As shown in Fig. 1b, a pulley coupler is adopted to increase the coupling length and ensure sufficient coupling between the ring and the bus waveguide, which are separated by a gap of 50 nm. To ensure precise control of the mask pattern close to the coupling section, different exposure doses are employed for the WGM resonator near and far from the pulley coupling structure to alleviate the proximity effect of electron beam lithography (EBL).

The deeply etched waveguide with grating holes is formed by a single-step inductively coupled plasma (ICP) dry etching process using a mixture of CH₄ and H₂. This process is made possible by taking advantage of the lag effect, i.e., the etch rate is dependent on the mask opening. Thereby, the etch rate within the grating holes is lower than in the open area. By adjusting the size of the grating holes and tuning the dry etching conditions, e.g., the gas ratio or the ICP power, precise control of the etching depth can be guaranteed²⁷. As a result, the MQW layer beneath the grating region remains intact, thus ensuring low transmission loss in the WGM resonator.

Reference

- Allen, L., Beijersbergen, W., Spreeuw, R. J. C. & Woerdman, J. P. Orbital angular momentum of light and the transformation of Laguerre-Gaussian laser modes. *Phys. Rev. A* **45**, 8185-8190 (1992).
- Yao, A. M., Padgett, M. J. Orbital angular momentum: origins, behavior and applications. *Adv. Opt. Photonics* **3**, 161-204 (2011).
- Molina-Terriza, G., Torres, J. P. & Torner, L. Twisted photons. *Nat. Phys.* **3**, 305-310 (2007).
- Wang, J. *et al.* Terabit free-space data transmission employing orbital angular momentum multiplexing. *Nat. Photonics* **6**, 488-496 (2012).
- Bozinovic, N. *et al.* Terabit-scale orbital angular momentum mode division multiplexing in fibers. *Science* **340**, 1545-1548 (2013).
- Willner, A. E. *et al.* Optical communications using orbital angular momentum beams. *Adv. Opt. Photonics* **7**, 66-106 (2015).
- Franke-Arnold, S., Allen, L. & Padgett, M. Advances in optical angular momentum. *Laser Photon. Rev.* **2**, 299-313 (2008).
- Padgett, M., Orbital angular momentum 25 years on. *Opt. Express* **25**, 11265-11274 (2017).
- He, H., Friese, M. E. J., Heckenberg, N. R. & Rubinsztein-Dunlop, H. Direct observation of transfer of angular momentum to absorptive particles from a laser beam with a phase singularity. *Phys. Rev. Lett.* **75**, 826-829 (1995).
- Grier, D. G. A revolution in optical manipulation. *Nature* **424**, 810-816 (2003).
- Padgett, M. & Bowman, R. Tweezers with a twist. *Nat. Photonics* **5**, 343-348 (2011).
- Fürhapter, S., Jesacher, A., Bernet, S., & Ritsch-Marte, M. Spiral interferometry. *Opt. Lett.* **30**, 1953-1955 (2005).
- Torner, L., Torres, J. P. & Carrasco, S. Digital spiral imaging. *Opt. Express* **13**, 873-881 (2005).
- Mair, A., Vaziri, A., Weihs, G. & Zeilinger, A. Entanglement of the orbital angular momentum states of photons. *Nature* **412**, 313-316 (2001).
- Leach, J. *et al.* Quantum correlations in optical angle-orbital angular momentum variables. *Science* **329**, 662-665 (2010).
- Beijersbergen, M. W., Coerwinkel, R. P. C., Kristensen, M., & Woerdman, J. P. Helical-wavefront laser beams produced with a spiral phaseplate. *Opt. Commun.* **112**, 321-327 (1994).
- Beijersbergen, M. W., Allen, L., Van der Veen, H. E. L. O., & Woerdman, J. P. Astigmatic laser mode converters and transfer of orbital angular momentum. *Opt. Commun.* **96**, 123-132 (1993).
- Bazhenov, V. Y., Vasnetsov, M. V., & Soskin, M. S. Laser beams with screw dislocations in their wavefronts. *Jetp Lett.* **52**, 429-431 (1990).
- Cai, X. *et al.* Integrated compact optical vortex beam emitters. *Science* **338**, 363-366 (2012).
- Doerr, C. R. & Buhl, L. L. Circular grating coupler for creating focused azimuthally and radially polarized beams. *Opt. Lett.* **36**, 1209-1211 (2011).
- Sun, J., Yaacobi, A., Moresco, M., Coolbaugh, D. D., & Watts, M. R. Integrated continuously tunable optical orbital angular momentum generator. *CLEO: 2015 Postdeadline Paper Digest, (OSA)*, paper JTh5A.5 (2015).
- Wang, Y. *et al.* Integrated photonic emitter with a wide switching range of orbital angular momentum modes. *Sci. Rep.* **6**, (2016).
- Li, H. *et al.* Orbital angular momentum vertical-cavity surface-emitting lasers. *Optica* **2**, 547-552 (2015).
- Miao, P. *et al.* Orbital angular momentum microlaser. *Science* **353**(6298), 464-467 (2016).
- Sun, C. *et al.* Analysis of OAM Mode Purity of Integrated Optical Vortex Beam Emitters. *IEEE Photon. J.* **9**, 1-7 (2017).
- Sun, C. *et al.* Fabrication and packaging of 40-Gb/s AlGaInAs multiple-quantum-well electroabsorption modulated lasers based on identical epitaxial layer scheme. *J. Lightwave Technol.* **26**, 1464-1471 (2008).
- See supplementary information.
- Moreno, I., Davis, J. A., Ruiz, I., & Cottrell, D. M. Decomposition of radially and azimuthally polarized beams using a circular-polarization and vortex-sensing diffraction grating. *Opt. Express* **18**, 7173-7183 (2010).
- Strain, M. J. *et al.* Fast electrical switching of orbital angular momentum modes using ultra-compact integrated vortex emitters. *Nat. Commun.* **5**, 4856 (2014).
- Gibson, G. *et al.* Free-space information transfer using light beams carrying orbital angular momentum. *Opt. Express*, **12**, 5448-5456 (2004).
- Yu, S., Cai, X., & Zhang, N. High index contrast integrated optics in the cylindrical coordinate. *Proc. SPIE* **9372**, 937203(2015).

Author contributions

J.Z. and C.S. designed the devices. J.Z. carried out the fabrication. Y.X., C.Y., T.T. and Y.N. contributed to the fabrication. J.Z., C.S., S.L. and X.C. performed the measurements. All of the authors contributed to the data analysis and authorship of the manuscript. C.S and S.Y. developed and supervised the project.

Additional information

Competing financial interests: The authors declare no competing financial interests.